### Title

Evidence of substrate binding and product release via belt-sulfur mobilization of the nitrogenase cofactor




### Journal

Nature Catalysis, 5(5)

### ISSN

2520-1158



### Authors

Lee, Chi Chung
Kang, Wonchull
Jasniewski, Andrew J
et al.



### Publication Date

2022-05-01

### DOI

10.1038/s41929-022-00782-7

Peer reviewed

Published in final edited form as:

*Nat Catal*. 2022 May ; 5(5): 443–454. doi:10.1038/s41929-022-00782-7.

# Evidence of substrate binding and product release via belt-sulfur mobilization of the nitrogenase cofactor

**Chi Chung Lee**[1], **Wonchull Kang**[1,2], **Andrew J. Jasniewski**[1], **Martin T. Stiebritz**[1], **Kazuki Tanifuji**[1,3], **Markus W. Ribbe**[1,4,*], **Yilin Hu**[1,*]

[1]Department of Molecular Biology and Biochemistry, University of California, Irvine, CA 92697-3900

[2]Department of Chemistry, College of Natural Sciences, Soongsil University, Seoul 06978, Republic of Korea

[3]Institute for Chemical Research, Kyoto University, Gokasho, Uji, Kyoto 611-0011, Japan

[4]Department of Chemistry, University of California, Irvine, CA 92697-2025

## Abstract

The Mo-nitrogenase catalyses the ambient reduction of $N_2$ to $NH_3$ at the M-cluster, a complex cofactor that comprises two metal-sulphur partial cubanes ligated by an interstitial carbide and three belt-sulphurs. A recent crystallographic study suggests binding of $N_2$ via displacement of the belt-sulphur(s) of the M-cluster upon turnover. However, the direct proof of $N_2$ binding and belt-sulphur mobilization during catalysis remains elusive. Here we show that $N_2$ is captured on the M-cluster via electron- and sulphur-depletion, and that the $N_2$-captured state is catalytically competent in generating $NH_3$. Moreover, we demonstrate that product release only occurs when sulphite is supplied along with a reductant, that sulphite is inserted as sulphide into the belt-sulphur displaced positions, and that there is a dynamic in-and-out of the belt-sulphurs during catalysis. Together, these results establish the mobilization of the cofactor belt-sulphurs as a crucial, yet overlooked, mechanistic element of the nitrogenase reaction.

## Graphical Abstract



*Corresponding authors: mribbe@uci.edu, yilinh@uci.edu.

Author Contributions

C.C.L, W.K., A.J.J., M.T.S., K.T, M.W.R. and Y.H. designed experiments. C.C.L, W.K., A.J.J., M.T.S., K.T, M.W.R. and Y.H. analysed data. C.C.L, W.K., A.J.J., M.T.S. and K.T. performed experiments. M.W.R. and Y.H. wrote the manuscript with input from all authors.

Competing Interests

The authors declare no competing interests.

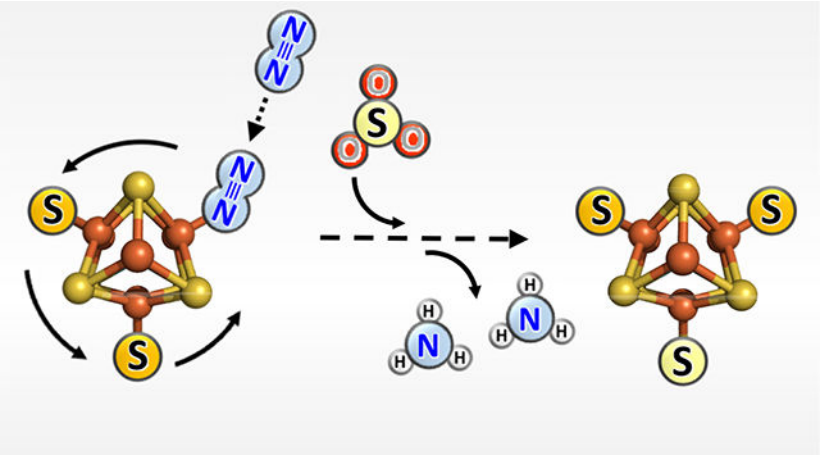


## Introduction

Nitrogenase is a complex metalloenzyme that bears significant relevance to the agronomy-, environment- and energy-related areas.[1–4] Best known for its role in catalysing the ambient conversion of the atmospheric $N_2$ to the bioavailable $NH_3$ as a key step in the global nitrogen cycle,[1] nitrogenase can also reduce CO and $CO_2$ to hydrocarbons (*e.g.*, $CH_4$, $C_2H_6$, $C_3H_8$) in ambient reactions that mimic the industrial Fischer-Tropsch process for carbon fuel production.[5,6] Other than $N_2$ and CO, nitrogenase is capable of reducing a wide variety of alternative substrates, including $C_2H_2$, $CN^-$, $N_3^-$ and $H^+$,[4] further illustrating the catalytic versatility of this important metalloenzyme. Catalysis by the conventional molybdenum (Mo) nitrogenase is accomplished by a two-component system that utilizes a reductase component to deliver electrons to a catalytic component for substrate reduction.[1–4,7,8] The reductase component, designated the iron (Fe) protein, is a homodimer containing a subunit-bridging $[Fe_4S_4]$ cluster and an ATP-binding site within each subunit; whereas the catalytic component, termed the molybdenum iron (MoFe) protein, is an $\alpha_2\beta_2$-heterotetramer containing a P-cluster ($[Fe_8S_7]$) at each α/β-subunit interface and an M-cluster (or FeMoco; [(*R*-homocitrate)$MoFe_7S_9C$]) within each α-subunit.[9,10] During substrate turnover, the two component proteins of Mo-nitrogenase form a function complex with each other, enabling ATP-dependent electron transfer from the $[Fe_4S_4]$ cluster of the Fe protein, via the P-cluster, to the M-cluster of the MoFe protein, where substrate reduction takes place once a sufficient number of electrons is accumulated.[1–4]

The functional importance and innate complexity of nitrogenase have inspired generations of researchers to obtain a mechanistic description of the enzymatic $N_2$ reduction by this enzyme, with the Lowe-Thorneley model[11–14] being the best-known kinetic depiction of the intra-protein delivery of protons and electrons to the M-cluster for substrate binding, activation and reduction to date. Characterization of the substrate- or intermediate-bound states of nitrogenase, on the other hand, has proven to be exceptionally challenging due to the transient nature of these bound species.[15] Along this line of effort, freeze quench spectroscopic techniques, combined with genetic modifications of the active site of Mo-nitrogenase, have been used to characterize certain states of this enzyme that are of potential

relevance to catalysis.[7,11–14] A very important step toward obtaining a molecular depiction of the ligand-bound state of Mo-nitrogenase, however, came from a high-resolution crystal structure of a CO-bound form of MoFe protein, which revealed the presence of a $\mu_2$-CO ligand bridged between Fe2 and Fe6 of the M-cluster in place of a belt sulphur (S2B).[16] This observation was exciting, as it pointed to a mechanism involving the generation of a reactive Fe species via displacement of a belt-sulphur of the cofactor. Perhaps even more intriguingly, a follow-up crystallographic pulse-chase study using a Se-reporter at the S2B site illustrated a migration of the Se label in the belt region of the M-cluster upon turnover with $C_2H_2$,[17] suggesting a possible involvement of the entire belt region of the cofactor in catalysis.

Recently, we captured an $N_2$-bound state of MoFe protein (designated Av1*) by subjecting a nitrogenase-expressing culture that was actively performing $N_2$ fixation to cell lysis in the absence of an externally supplied electron source (*i.e.*, dithionite) and subsequently isolating the histidine-tagged MoFe protein in the absence of oxygen by a quick one-step purification procedure.[18] Contrary to the resting-state MoFe protein (designated Av1) that was isolated in the presence of dithionite, Av1* was trapped in a dormant $N_2$- or intermediate-bound state due to a withdrawal of electron flow to the M-cluster; yet, its activity could be fully restored in an *in vitro* activity assay, where it was combined with the Fe protein (designated Av2), ATP and dithionite. Crystallographic analysis of Av1* revealed oxidation of the P-clusters in both αβ-dimers to the two-electron-oxidized state ($P^{OX}$) (Supplementary Fig. 1a, b), suggesting a restricted electron flow from the P-cluster to the M-cluster that left the former in an electron-depleted state while permitting the latter to capture $N_2$ and/or intermediates under limited turnover conditions. Consistent with this suggestion, Av1* showed asymmetric displacements of a belt sulphur (S2B) in one of its M-clusters and two other belt sulphurs (S3A and S5A) in the other, as well as asymmetric elongations of the Mo-O7 and Mo-O5 bonds, respectively, in the S2B- and S3A/S5A-displaced M-clusters that switched the Mo-homocitrate ligation in both cofactors from bidentate to monodentate (Supplementary Fig. 2a, b). The belt-sulphur displacement in Av1* was further illustrated by the return of sulphurs to the cofactor belt regions upon turnover of Av1* in the presence of Av2, ATP and dithionite, resulting in a reactivated protein species (designated Av1*(TOD); TOD=TurnOver with Dithionite) that was indistinguishable from the resting-state Av1 (Supplementary Fig. 2c–f). Moreover, modelling of small molecules at the sulphur-displaced positions of the cofactors in Av1*, supported by the observation of $^{15}N_2$ release from the acid-quenched Av1* that was isolated from the $^{15}N_2$-grown culture, led to the proposal of belt-sulphur displacement with dinitrogen species upon turnover. Taken together, our observation that all three belt-sulphur sites are involved in catalysis is consistent with the previously observed migration of a Se-reporter in the cofactor belt region, leading to the proposal of a mechanism involving asynchronous rotations of the M-clusters in the two αβ-dimers of the MoFe protein that allow a stepwise reduction of $N_2$ at the three belt-sulphur sites to occur asynchronously in the two M-clusters (Supplementary Fig. 3).[18]

Despite the initial structural insights into a plausible catalytic mechanism involving belt-sulphur displacement, the direct evidence of $N_2$ binding and belt-sulphur mobilization during nitrogenase catalysis is yet to be acquired. Here we use a combination of biochemical, analytical, spectroscopic, and structural approaches to demonstrate that $N_2$

is captured on the M-cluster under electron- and sulphur-depleted conditions, and that such a $N_2$-captured state is catalytically relevant and capable of generating $NH_3$ upon turnover. Furthermore, we show that product release only occurs in the presence of sulphite and reductant, that sulphite is inserted as sulphide into the belt-sulphur displaced locations, and that there is a dynamic mobilization of the belt-sulphurs during catalysis. These observations collectively point to the mobilization of belt-sulphurs as a previously unidentified key element of the nitrogenase mechanism.

## Results

### Binding and conversion of $N_2$ to $NH_3$ via single turnover

To obtain further evidence for $N_2$-binding in Av1*, we first examined whether Av1* could incorporate D into the two-electron reduction products, such as $H_2$ or $C_2H_4$, upon turnover of $H^+$ or $C_2H_2$ in the presence of $D_2$. Previous studies have revealed formation of HD upon turnover by Av1 in the presence of $D_2$ and $N_2$, as well as a lack of appreciable production of TOH upon turnover by Av1 in the presence of $T_2$ and $N_2$,[19–23] pointing to an $N_2$-dependent HD exchange that routes via an $N_2$-bound/activated state of Av1 rather than via a simple solvent exchange. Consistent with earlier suggestions of metal hydride formation at the active site of Av1 during turnover,[19,25,26] a reductive elimination mechanism[7,27] has been proposed to rationalize the H/D isotope exchange achieved by $N_2$-bound/activated Av1 under $D_2$, which involves displacement of $N_2$ from the active-site cofactor of Av1 (designated *E*) upon binding of $D_2$ as an $E(D^-)_2$ intermediate, followed by a reversal of Av1 to the starting, un-activated state (designated $E_0$) concomitant with the formation of deuterated $H_2$ in the absence of additional substrate(s), or the formation of deuterated $C_2H_4$ upon turnover of $C_2H_2$, in $H_2O$-based reactions (Supplementary Fig. 4). Subsequent gas chromatography (GC) analysis of products resulting from turnover under $D_2/C_2H_2$ and $N_2/D_2/C_2H_2$, respectively, revealed formation of un-deuterated $C_2H_4$ in the case of the former (*i.e.*, without $N_2$) that contrasted formation of a minor yield of $C_2H_2D_2$ and, more abundantly, $C_2H_3D$, in the case of the latter (*i.e.*, with $N_2$).[27]

Using $C_2H_3D$ as a more reliable marker for detecting D incorporation, we conducted combined GC and gas chromatography-mass spectrometry (GC–MS) analyses (Fig. 1a, b) and obtained results on Av1 controls in agreement with those from the previous GC analysis.[27] Specifically, turnover by Av1 under $D_2/C_2H_2$ generated a product with the same GC retention time (Fig. 1a, solid grey) and GC–MS fragmentation pattern (Fig. 1b, grey bars) as those of the un-deuterated $C_2H_4$ standard (Fig. 1a, dashed black; Fig. 1b, black bars); whereas turnover by Av1 under $N_2/D_2/C_2H_2$ generated a product with a distinct shift in the GC retention time (Fig. 1a, solid blue) and a clear change of the GC–MS fragmentation pattern—particularly with respect to the peak at $m/z$=29—that indicated formation of $C_2H_3D$ (Fig. 1b, blue bars). Excitingly, like turnover by Av1 under $N_2/D_2/C_2H_2$, turnover by Av1* under $D_2/C_2H_2$—without addition of any 'extra' $N_2$—yielded a product with a shift in the GC retention time (Fig. 1a, solid brown) and a change of the GC–MS fragmentation pattern (Fig. 1b, brown bars) consistent with the formation of $C_2H_3D$. Given the dependence of D incorporation on an $N_2$-bound state of the cofactor, this observation provides compelling evidence for the binding of $N_2$ to the active site of

Av1*. More importantly, the striking similarity in the fragmentation patterns of the products generated by turnover with Av1* under $D_2/C_2H_2$ and turnover with Av1 under $N_2/D_2/C_2H_2$ points to Av1* as an activated, $N_2$-bound intermediate that appears during the normal turnover with Av1 under $N_2$.

The catalytic relevance of Av1* was further examined by monitoring ammonia formation from a direct turnover of the $N_2$ species associated with Av1*. Detection of $NH_3$ generated by such a single-turnover event has proven extremely challenging due to the lack of a sensitive technique for the low-yield $NH_3$ production, compounded further by a high background reading of $NH_3$ that is derived from protein degradation and ambient $NH_3$ contamination. Recently, an elegant frequency-selective nuclear magnetic resonance (NMR) method was developed to directly detect $NH_3$ (in the form of $NH_4^+$) in an electrolyte upon electrocatalytic $N_2$ reduction.[28] Using a pulse sequence composed of a hard 90° pulse and two gradient pulses surrounding the selective, Gaussian-shaped 180° pulse, this method was shown to be highly effective in minimizing solvent proton signals while specifically targeting the $NH_4^+$ signal, thereby allowing $^{14}N$ and $^{15}N$ to be distinguished as a 1:1:1 triplet and a 1:1 doublet, respectively, in the $^1H$ NMR spectrum based on a clear difference in their nuclear spins ($^{14}N$: $s$=1; $^{15}N$, $s$=1/2).[28] An adaption of this technique to our aqueous, protein-based systems led to the observation of a 1:1:1 triplet at 7.17 ppm that was assigned to $^{14}NH_4^+$ generated by the unbound, resting-state Av1 upon turnover with Av2, MgATP and dithionite under Ar (Fig. 1c, solid blue). Yet, this $^{14}NH_4^+$ signal was nearly indistinguishable in amplitude from that of the control assay comprising only Av2, MgATP and dithionite under Ar (Fig. 1c, dashed black) but almost absent from a second control assay containing only Av1, MgATP and dithionite under Ar (Fig. 1c, dashed blue). These observations collectively point to a strong stability of Av1—the catalytic component of nitrogenase—under turnover conditions while suggesting the amino groups of degraded Av2—the reductase component of nitrogenase that is well known for its instability, particularly with respect to its catalytic partner—as almost the sole origin of the $^{14}NH_4^+$ signal in the NMR spectrum of the turnover sample of Av1 (Fig. 1c, dashed black *vs.* dashed green).

Having established the $^{14}NH_4^+$ background reading under turnover conditions, we then prepared Av1* in the presence of $^{14}N_2$ and $^{15}N_2$ (designated $^{14}N_2$-Av1* and $^{15}N_2$-Av1*, respectively) and applied the frequency-selective NMR technique to these samples following turnover with Av2, MgATP and dithionite under Ar. What was immediately apparent was that $^{14}N_2$-Av1* yielded a 1:1:1 triplet of $^{14}NH_4^+$ (Fig. 1c, solid red) approximately twofold in amplitude compared to those of the unbound Av1 (Fig. 1c, solid blue) or the control (Fig. 1c, dashed green) upon turnover, suggesting a reduction of the Av1*-bound $^{14}N_2$ that contributed to the notable increase in the intensity of the $^{14}NH_4^+$ signal. Consistent with this suggestion, turnover of $^{15}N_2$-Av1* under the same conditions resulted in a distinct 1:1 doublet that originated from $^{15}NH_4^+$ (Fig. 1c, solid brown, '$^{15}NH_4^+$'), which conclusively demonstrated the presence of $N_2$ in Av1*. The 1:1:1 triplet that originated from $^{14}NH_4^+$ in the same $^{15}N_2$-Av1* sample (Fig. 1c, solid brown, '$^{14}NH_4^+$'), on the other hand, was comparable in amplitude to the background readings of the unbound Av1 sample (Fig. 1c, solid blue) and the control (Fig. 1c, dashed green), making it an excellent internal reference point for this experiment. It should be noted that while the frequency-selective NMR method was successfully applied to the quantitation of $NH_3$ produced by the electrochemical

reduction of $N_2$,[28] it is more suitable as a qualitative measure of the enzymatic $N_2$ reduction due to complications arising from an exceedingly low $NH_3$ yield relative to a very high $NH_3$ background of the enzymatic single-turnover event. Regardless, the conclusive NMR observation of $NH_4^+$ formation upon turnover firmly establishes Av1* as a catalytically relevant intermediate of $N_2$ reduction.

## Sulphur-dependent substrate binding and product release

To further investigate the $N_2$- and/or derivative-bound state of Av1*, we performed EPR analysis of the resting-state Av1, the $N_2$-bound Av1*, and the reactivated Av1*(TOD). As expected, Av1 displayed an M-cluster-specific $S = 3/2$ signal with $g$ values of 4.31, 3.67 and 2.01 (Fig. 2a). Compared to Av1, Av1* (Fig. 2b; also see Supplementary Fig. 5) displayed the $S = 3/2$ signal at only 54% intensity with slightly broadened lineshape (with $g$ values changed to 4.32, 3.66 in the $S = 3/2$ region); more excitingly, three previously unobserved features appeared in the $S = 1/2$ region of the spectrum of Av1* at $g = 2.22$, 2.01 and 1.88 (Fig. 2b), consistent with capture of dinitrogen species on the M-clusters of this protein species. Clearly distinct in temperature dependency, the features at $g = 2.22$ and 1.88 showed maximum intensities at 10 K; whereas the feature at $g = 2.01$ showed maximum intensity at 30 K (Fig. 2b, inset; Supplementary Fig. 5). Upon turnover of Av1* in dithionite, these additional features disappeared along with a full restoration of the $S = 3/2$ signal, resulting in a spectrum of Av1*(TOD) (Fig. 2c) that was indistinguishable from that of Av1 (Fig. 2a) in intensity, lineshape and temperature dependency, consistent with release of the bound dinitrogen species from the M-cluster under these conditions. This argument was further corroborated by our deuterium exchange and single-turnover experiments (see Fig. 1), as well as GC-MS analysis demonstrating the release of $^{15}N_2$ upon acid quenching of Av1* that was purified without dithionite from the $^{15}N_2$-grown culture of *A. vinelandii* (Fig. 2l); whereas in contrast, no $^{15}N_2$ release was detected upon acid quenching of the resting-state Av1 that was isolated with dithionite from the same $^{15}N_2$-grown culture (Fig. 2k) or the reactivated Av1*(TOD) that was prepared upon turnover of $^{15}N_2$-bound Av1* in the presence of dithionite (Fig. 2m).

The variations of the states of the M-clusters in Av1, Av1* and Av1*(TOD) could be correlated further with the changes in the oxidation states of the P-clusters in the three protein species. Accompanying the change of the M-cluster from the resting state to the $N_2$-bound state, the P-cluster was converted from the EPR-silent, all-ferrous $P^N$ state in Av1 (Fig. 2f) to the two-electron-oxidized $P^{OX}$ state in Av1* that was signified by a parallel-mode $g = 11.8$ signal (Fig. 2g), consistent with transfer of electrons from the P-cluster to the M-cluster in Av1* that allowed capture of $N_2$ or intermediates at the cofactor site. Following turnover in dithionite, however, the P-cluster reverted from the oxidized state ($P^{OX}$) in Av1* back to the reduced state ($P^N$) in Av1*(TOD) (Fig. 2h), which would account for a conversion of this protein species to the resting state when a sufficient supply of electrons (*e.g.*, provided by dithionite) rendered the P-cluster reduced and capable of delivering electrons to the M-cluster. Taken together, the results from our EPR experiments (Fig. 2a–c) align well with those from our biochemical (Fig. 2k–m) and crystallographic analyses (Supplementary Figs. 1 and 2)[18] of Av1* and provide strong evidence for the capture of turnover-related dinitrogen species at the cofactor site of Av1*.

Interestingly, while Av1* was capable of reducing $C_2H_2$, $H^+$ and $N_2$ to the respective products when combined with Av2, ATP and dithionite in an *in vitro* activity assay, no product could be detected in the same *in vitro* assay upon substitution of dithionite with Eu(II)-EGTA, a sulfur-free reductant (Fig. 3a, −S). The discrepancy between the sulphur-containing (*i.e.*, dithionite) and sulphur-free [*i.e.*, Eu(II)-EGTA] reductants points to a dual role of dithionite in nitrogenase catalysis, supplying electrons to enable substrate reduction while providing sulphurs to facilitate product release. Such an argument would be consistent with the return of belt sulphurs in Av1*(TOD) concomitant with the restoration of the turnover capability of this protein species.[18] Given the known ability of dithionite to breakdown into three physiological relevant sulphur species, sulphide ($S^{2-}$), sulphite ($SO_3^{2-}$) and sulphate ($SO_4^{2-}$), we examined the ability of these sulphur species to drive the activity of nitrogenase along with the sulphur-free reductant, Eu(II)-EGTA. Our results clearly demonstrated that while $S^{2-}$ and $SO_4^{2-}$ were unable to fulfil this task (Fig. 3a, $+S^{2-}$, $+SO_4^{2-}$), $SO_3^{2-}$ was capable of restoring the activity of Av1* in combination with Eu(II)-EGTA, Av2 and ATP (Fig. 3a, $+SO_3^{2-}$). The ability of $SO_3^{2-}$-type species to drive the nitrogenase reaction was reaffirmed by the observation of comparable $C_2H_2$-, $H^+$- and $N_2$-reducing activities upon substitution of $SeO_3^{2-}$ for $SO_3^{2-}$ in the same *in vitro* activity assay (Fig. 3a, $+SeO_3^{2-}$), although the overall activity of $N_2$ reduction and the $NH_3/H_2$ ratio were lower in the $SeO_3^{2-}$-based assay than those in the $SO_3^{2-}$-based assay. The dependence of nitrogenase activity on $SO_3^{2-}$-type species was further illustrated when the $C_2H_2$-reducing activity was titrated against increasing concentrations of $SO_3^{2-}$ or $SeO_3^{2-}$ (Fig. 3b), although the two species displayed distinct titration patterns: in the case of the former, the activity reached the maximum at 2 mM $SO_3^{2-}$ and roughly plateaued beyond this concentration; whereas in the case of the latter, the activity rapidly peaked at 0.2 mM $SeO_3^{2-}$ but decreased by ~4 fold when the concentration of $SeO_3^{2-}$ was increased to 10 mM (Fig. 3b). Of note, the reaction of $C_2H_2$-reduction by Av1* displayed a nearly indistinguishable time-dependence when it was driven by 2 mM $SO_3^{2-}$ (Fig. 3c, $SO_3^{2-}$) or a nitrogenase-free cell extract (Fig. 3c, NFE) in the presence of Eu(II)-EGTA, particularly with regard to the lag phase within the first 5 min of the reaction. This observation implies the presence of $SO_3^{2-}$ or an equivalent sulphur species in the cell that could drive the nitrogenase reaction alongside the physiological electron donors *in vivo*, which is not surprising given that $SO_3^{2-}$ represents one of the central hubs of sulphur metabolism in all classic nitrogen-fixing microorganisms (see Supplementary Fig. 6).

Importantly, the protein species re-isolated upon turnover of the $^{15}N_2$-bound Av1* with Av2, ATP, and excess Eu(II)-EGTA and $SO_3^{2-}$ (designated Av1*(TOS); TOS=TurnOver with Sulphite) adopted an M-cluster-specific $S = 3/2$ signal (Fig. 2d) of indistinguishable intensity, lineshape and temperature dependency from the $S = 3/2$ signals displayed by the resting-state Av1 (Fig. 2a) and the dithionite-reactivated Av1*(TOD) (Fig. 2c). Consistent with the presence of its M-cluster in a substrate- or intermediate-free state, no $^{15}N_2$ release was detected from Av1*(TOD) upon acid quenching (Fig. 2n); moreover, the P-cluster of Av1*(TOS) (Fig. 2i) adopted the same EPR-silent, reduced $P^N$ state as those in Av1 (Fig. 2f) and Av1(TOD) (Fig. 2h), aligning well with the resting state of the M-cluster in Av1*(TOS). As observed in the activity assays, the ability of $SO_3^{2-}$-type species to reactivate Av1* was illustrated by the observation that the protein species re-isolated upon

turnover of the $^{15}N_2$-bound Av1* with Av2, ATP, Eu(II)-EGTA and $SeO_3^{2-}$ (designated Av1*(TOSe); TOSe=TurnOver in Selenite) had the M-cluster-specific, resting-state $S$ = 3/2 signal largely restored (Fig. 2e). However, the resting-state features at $g$ = 4.31 and 3.67 were not completely recovered, and the dinitrogen-species-related feature at $g$ = 2.01 was still more pronounced, in the spectrum of Av1*(TOSe) (Fig. 2e) as compared to their respective counterparts in the spectra of Av1, Av1*(TOD) and Av1*(TOS) (Fig. 2a, c, d). In line with the observation of an incomplete restoration of its M-cluster to the resting state, a minor amount of $^{15}N_2$ release (6% relative to that released by Av1*) could still be detected upon acid quenching of Av1*(TOSe) (Fig. 2o). Additionally, a small portion (17%) of the P-cluster of this protein species retained the $g$ = 11.8 feature that was characteristic of the $P^{OX}$ state (Fig. 2j), implying a less efficient transfer of electrons from the P-cluster to the M-cluster that rendered the latter more oxidized than its EPR-silent counterpart in the resting-state Av1 or reactivated Av1*(TOD) and Av1*(TOS) (Fig. 2f, h, i). Such a $SeO_3^{2-}$-associated change in the oxidation state of the M-cluster did not seem to affect the reduction of easier substrates, such as $C_2H_2$ and $H_2$; however, it had an impact on the reduction of more difficult substrates like $N_2$ (Fig. 3a), likely due to the requirement of a more reduced state of the M-cluster for this reactivity.

## Dynamic belt-sulphur mobilization during turnover

The observation that a combination of Eu(II)-EGTA and $SO_3^{2-}$ acts as an equivalent of dithionite to promote product release (see Fig. 3) and reactivate Av1* to the resting-state, belt-sulphur-replete conformation of Av1*(TOS) (see Fig. 2) points to $SO_3^{2-}$ as an effective sulphur source to displace the bound dinitrogen species and refill the belt-sulphur positions in the M-clusters of Av1* upon turnover. To obtain structural evidence for this argument, we crystallized Av1*(TOS) under anaerobic conditions and obtained brown crystals that diffracted to a resolution of 1.65 Å (Fig. 4; Supplementary Fig. 7; Supplementary Tables 1, 2). The structure of Av1*(TOS) is indistinguishable from those of the resting-state Av1 and the dithionite-reactivated Av1*(TOD), with both of its P-clusters adopting the conformation of the reduced $P^N$ state (Fig. 4a, b) and both of its M-clusters having all three belt-sulphurs in place and the homocitrate ligand assuming bidentate ligation to Mo via its O5 and O7 atoms (Fig. 4c–f). These observations are consistent with the bound dinitrogen species of Av1* being turned over and subsequently released from the M-clusters in the presence of sufficient electrons and sulphurs, as well as the inability of the M-clusters to recapture $N_2$ or intermediates under these conditions, which inadvertently reverts both P- and M-clusters in Av1*(TOS) to the resting-state conformations. Notably, the sulphur species in Av1*(TOS) show the same pattern of anomalous densities as those of their invariable S2B in Chain-A and S3A/S5A in Chain-C), once again highlighting the deviation of the anomalous densities of the displaced belt-sulphur sites (S2B, S3A, S5A) in Av1* from the conserved pattern of the anomalous densities of the invariable sulphurs at the corresponding positions (Fig. 5a). The clear distinctions between the sulphur anomalous densities (Fig. 5a), EPR features (see Fig. 2) and catalytic activities (see Fig. 3) of Av1* and Av1*(TOS) not only provide strong validation for the belt-sulphur displacement with dinitrogen species in the M-clusters of Av1*,[18] but also point to a plausible mechanism of product release via incorporation of $SO_3^{2-}$ as $S^{2-}$ at the displaced belt-sulphur position of Av1* that renders the resulting Av1*(TOS) in a belt-sulphur-replete conformation.

To trace the fate of $SO_3^{2-}$ during catalysis, Av1* was subjected to turnover with Av2, ATP, Eu(II)-EGTA and the isotopically labelled $^{34}SO_3^{2-}$ for 10 min and re-isolated from the incubation mixture, resulting in a protein species designated Av1*($TO^{34}S$). Subsequently, Av1*($TO^{34}S$) was subjected to turnover with Av2, ATP, Eu(II)-EGTA and unlabelled $^{32}SO_3^{2-}$ for 60 min and re-isolated again from the incubation mixture, resulting in a protein species designated Av1*($TO^{34}S$)$^{60\ min}$. Av1*($TO^{34}S$) and Av1*($TO^{34}S$)$^{60\ min}$ were then subjected to acid quenching and analysed by gas chromatograph-mass spectrometry (GC-MS) for the release of acid-labile cluster sulphides as $H_2S$. Interestingly, $H_2{}^{34}S$ was detected upon acid quenching of Av1*($TO^{34}S$) (Fig. 5b, trace 3), but not upon acid quenching of Av1*($TO^{34}S$)$^{60\ min}$ (Fig. 5b, trace 4), suggesting incorporation of the $^{34}S$ label in Av1*($TO^{34}S$) upon turnover with $^{34}SO_3^{2-}$, followed by substitution of unlabelled $^{32}S$ for the $^{34}S$ label in Av1*($TO^{34}S$)$^{60\ min}$ upon turnover with $^{32}SO_3^{2-}$, resulting in a species equivalent to Av1*(TOS) (Fig. 5b, trace 2). The origin of $H_2{}^{34}S$ was further traced to the acid-labile sulphides of the M-cluster, as $H_2{}^{34}S$ was detected upon acid quenching of the M-cluster extracted from Av1*($TO^{34}S$) (Fig. 5c, trace 3). The release of the cofactor-associated $^{34}S^{2-}$ as $H_2{}^{34}S$ upon acid quenching is consistent with our structural observation of incorporation of $SO_3^{2-}$ as $S^{2-}$ in the belt region of Av1*(TOS); whereas the in-and-out of the $^{34}S$ label upon sequential turnover of Av1* with $^{34}SO_3^{2-}$ and $^{32}SO_3^{2-}$ highlights a crucial role of belt-sulphur mobilization during catalysis.

In parallel to the isotope labelling experiments, Se was used both as an analytic tool and as a spectroscopic handle to monitor the mobilization of $SO_3^{2-}$ as a source of belt-sulphurs under turnover conditions. The experiments using Se as a marker for belt-sulphur involved turnover of Av1* under $N_2$ for 10 min with Av2, ATP, $SeO_3^{2-}$ and either low or high fluxes of electrons derived from Eu(II)-EGTA, and re-isolation of protein species from the incubation mixture, resulting in protein species designated Av1*(TOSe)$^{N2}$ (prepared under low flux conditions) or Av1*(TOSe) (prepared under high flux conditions) that should mimic Av1* and Av1(TOS), respectively (see Methods and Supplementary Methods for experimental details). Subsequent inductively coupled plasma optical emission spectrometry (ICP-OES) analysis of the M-clusters extracted from these protein species revealed Se/Mo ratios of 1.76±0.39 and 2.97±0.48, respectively, for Av1*(TOSe)$^{N2}$ and Av1*(TOSe) (Fig. 5d). Strikingly, the Se/Mo ratio of Av1*(TOSe)$^{N2}$ resembles the belt-S/Mo ratios derived from the crystal structures of $N_2$-bound Av1* (with its two M-clusters containing 2 Mo and 3 belt-S), thereby providing strong, albeit indirect support for the assignment of ligand binding via belt-S displacement in these structures. In comparison, the Se/Mo ratio of Av1*(TOSe) reflects the belt-S/Mo ratio of the resting-state Av1 (with its two M-clusters containing 2 Mo and 6 belt-S), consistent with a return of the belt-S (or belt-Se) upon turnover of Av1* with $SeO_3^{2-}$ that was also observed in our EPR and activity analyses (see Figs. 2 and 3).

With Av1*(TOSe) confirmed to be labelled with Se at all belt-S sites of its M-clusters, we subjected this protein to turnover with Av2, ATP, Eu(II)-EGTA and $SO_3^{2-}$ for 5 and 60 min, respectively, and re-isolated the protein species—designated Av1*(TOSe)$^{5\ min}$ and Av1*(TOSe)$^{60\ min}$—from the incubation mixtures. Subsequently, we performed Fe and Se K-edge XAS/EXAFS analyses of Av1*(TOSe), Av1*(TOSe)$^{5\ min}$ and Av1*(TOSe)$^{60\ min}$

to examine the overall geometry and Se incorporation of the M-clusters in these protein species (Fig. 6; also see Supplementary Tables 3–9). In general, the Fe K-edge data of Av1*(TOSe), Av1*(TOSe)$^{5\ min}$ and Av1*(TOSe)$^{60\ min}$ (Fig. 6a–d) are rather similar to one another, suggesting an overall structural conservation of the M-cluster during turnover. However, there are clear distinctions between the protein samples prepared with shorter and longer chase with $SO_3^{2-}$. Specifically, the FT spectrum of Av1*(TOSe)$^{5\ min}$ (Fig. 6c, blue) is nearly identical to that of Av1*(TOSe) (Fig. 6c, black), with the feature at R+Δ~2.3 Å that originates from Fe---Fe and Fe---Mo scattering showing a slightly higher intensity than the feature at R+Δ~1.8 Å that originates primarily from Fe-S scattering. In contrast, the FT spectrum of Av1*(TOSe)$^{60\ min}$ (Fig. 6c, red) has a set of intensities for the two prominent features at R+Δ~2.3 Å and ~1.8 Å that more closely resemble the previously published data for the belt-sulphur-replete, resting-state Av1, with a greater ratio between the intensities of the R+Δ~2.3 Å and ~1.8 Å features than those in the FT spectra of Av1*(TOSe) and Av1*(TOSe)$^{5\ min}$. The fact that the overall structure of the M-cluster in Av1*(TOSe)$^{60\ min}$ resembles that of its counterpart in the belt-sulphur-replete, resting-state Av1 provides the first hint towards a substitution of S for Se upon turnover of Av1*(TOSe) with $SO_3^{2-}$ for a certain length of time.

Subsequent Se K-edge analyses of Av1*(TOSe), Av1*(TOSe)$^{5\ min}$ and Av1*(TOSe)$^{60\ min}$ (Fig. 6e–g) allowed direct assessment of the Se contents of the M-clusters in these protein species. EXAFS spectra were obtained for Av1*(TOSe) (Fig. 6e, f, black) and Av1*(TOSe)$^{5\ min}$ (Fig. 6e, f, blue); however, Av1*(TOSe)$^{60\ min}$ contained such a low concentration of Se that only normalized fluorescence around the rising edge could be obtained (Fig. 6g, red). The FT spectra of Av1*(TOSe) and Av1*(TOSe)$^{5\ min}$ are highly similar, both showing a large prominent feature at R+Δ~2 Å that is consistent with Se–Fe distances at ~2.4 Å (Fig. 6d, black, blue). Such a feature is the primary contributor to both FT spectra, and the Se–Fe distances are consistent with a $Se^{2-}$-type incorporation into the M-clusters of both Av1*(TOSe) and Av1*(TOSe)$^{5\ min}$. It is interesting to note that additional Se–O scatterers are required to best fit the data of both Av1*(TOSe) and Av1*(TOSe)$^{5\ min}$ around R+Δ~1.9 Å and 2.1 Å, which could be interpreted as the presence of a mixture of cluster-bound $Se^{2-}$ and reduced $SeO_x$ (x=1 or 2) species in these samples. The more oxidized nature of the Se species than its S counterpart could account for the differences in the EPR features and catalytic activities of Av1* upon turnover with $SO_3^{2-}$ and $SeO_3^{2-}$ (see Figs. 2 and 3). More importantly, the composition of the Se species changes over time until it is barely observable in Av1*(TOSe)$^{60\ min}$ (Fig. 6g). This observation again illustrates that the M-cluster-bound Se species is chased off and replaced with S when subjected to longer turnover with $SO_3^{2-}$.

The results from our XAS/EXAFS $SO_3^{2-}$-chase experiments align well with those from the previous crystallographic pulse-chase study that illustrated the eventual disappearance of the migrating Se label from the belt region of the M-cluster over a certain period of turnover.[17] These observations collectively contradict an earlier proposal that a certain belt $S^{2-}$ ion always returns to its original position after being displaced by substrate during turnover;[29] instead, they point to a loss of the original belt $S^{2-}$ ion due to the incorporation of an external sulphur source as a new $S^{2-}$ ion at the displaced belt position. This argument is supported by our observation of 21% of electrons that were unaccounted for when

comparing the electron input (from the pre-reduced electron donor, Av2) and electron output (in the reduced products, $NH_3$ and $H_2$) in the reaction of $N_2$-reduction by Av1* with $SO_3^{2-}$ under limited, low-flux turnover conditions (Supplementary Fig. 8a; also see Methods and Supplementary Methods for experimental details), which could be routed towards a reductive incorporation of $SO_3^{2-}$ as new belt $S^{2-}$ ions. In the context of our previously proposed mechanistic model of stepwise reduction of $N_2$ at S3A, S2B and S5A via cluster rotation,[18] one plausible scenario for the dynamic exchange between $SO_3^{2-}$ and $S^{2-}$ in this process would involve release of $NH_3$ at the S5A site upon displacement with a $SO_3^{2-}$-derived $S^{2-}$ species, followed by rotation of the M-cluster that brings the newly incorporated $S^{2-}$ species to the S3A site for its subsequent displacement upon binding of $N_2$ (Supplementary Fig. 3).

To test whether it is thermodynamically feasible for $SO_3^{2-}$ to displace the product $NH_3$ from the S5A site of the M-cluster, we performed DFT calculations of the binding affinity of $SO_3^{2-}$ or $NH_3$ as a ligand to an M-cluster model lacking a belt $S^{2-}$ ion at the S5A site (designated M-cluster$^{\Delta S5A}$). For each ligand (designated L; L=$SO_3^{2-}$ or $NH_3$), we evaluated the energetics of the following reaction:

$$\text{M-cluster}^{\Delta S5A} + \text{L} \leftrightarrow \text{M-cluster}^{\Delta S5A} - \text{L} \quad (1)$$

Given the higher structural versatility of $SO_3^{2-}$ than $NH_3$, different starting configurations of $SO_3^{2-}$ were considered, which converged to two distinct coordination scenarios (Fig. 7a). One of them has $SO_3^{2-}$ bridged via its S atom and one of its O atoms between a pair of Fe atoms (Fe3, Fe7) across the belt of the M-cluster (Fig. 7a); whereas the other has $SO_3^{2-}$ bridged via two of its O atoms between the same pair of Fe atoms (Fig. 7b). While the former binding pattern (Fig. 7a, −76.2 kcal/mol) is somewhat less exothermic than the latter (Fig. 7b, −85.9 kcal/mol), in both cases, $SO_3^{2-}$ has a much higher affinity than $NH_3$ (Fig. 7c, −33.4 kcal/mol) for the S5A site of the M-cluster and, therefore, could readily displace $NH_3$ during catalysis. Upon release of $NH_3$, the subsequent reduction of $SO_3^{2-}$ to $S^{2-}$ at the free S5A site is thermodynamically favourable in both coordination scenarios (Fig. 7d, e), which involves coupled $e^-/H^+$ transfer to the cluster-bound $SO_3^{2-}$ species and removal of its O atoms as water until a belt $S^{2-}$ ion is regenerated on location.

## Conclusions

Taken together, our deuterium exchange, frequency-selective NMR, EPR and Se-labelling experiments provide compelling evidence for our structural assignment of Av1* as an $N_2$- or derivative-bound intermediate while firmly establishing the physiological relevance of Av1* to the turnover of $N_2$. Additionally, our enzymatic, crystallographic, XAS/EXAFS and DFT analyses reveal the requirement of a specific sulphur source along with electrons to drive the nitrogenase reactivity, thereby adding another twist to the mechanistic consideration of nitrogenase that has been historically focused solely on the successive addition of electrons to the M-cluster-bound substrate. The release of products only upon sulphur incorporation into the displaced belt-sulphur site of Av1*, accompanied by the loss of turnover-related EPR signals in this process, lends strong support to the successful capture of substrate and/or

intermediate on the M-cluster of Av1*.[18] More importantly, the ability of the belt sulphur to go in and out upon turnover with $SO_3^{2-}$ points to the possibility that an interconversion between a certain sulphur species (*e.g.*, $SO_3^{2-}$) and a belt-sulphur (*i.e.*, $S^{2-}$), which occurs concomitantly with the binding of $N_2$ via belt-sulphur displacement and, conversely, the release of $NH_3$ upon belt-sulphur incorporation (Supplementary Figs. 3 and 8b), as a crucial mechanistic element that has been left out of the equation of the nitrogenase reaction so far. The fact that $SO_3^{2-}$ must be supplied externally to drive the *in vitro* reactivity of Av1*, along with the observation that the belt-sulphur label is chased off Av1 upon turnover with $SO_3^{2-}$, suggests a plausible scenario under *in vivo* conditions in which the displaced belt-sulphur does not directly return to the M-cluster but instead enters a general sulphur pool in the cell where it could potentially be recycled as a belt-sulphur source for later use (Supplementary Figs. 3 and 8b). In theory, such a sulphur pool could support an *in situ* redox interconversion between $SO_3^{2-}$ and $S^{2-}$ at the belt location of the M-cluster, with the reductive half of this event fuelled by electrons supplied by Av2 and, conceivably, the oxidative half of this event coupled with $N_2$ reduction—directly or indirectly—given the six electrons involved in both reactions (Supplementary Fig. 8b). Moreover, the constant in-and-out of belt-sulphur may result in a frequent net loss of sulphur from the closed circle of $SO_3^{2-}/S^{2-}$ interconversion and thus require a refill of $SO_3^{2-}$. Such a hypothesis could account for the missing electrons in the electron inventory of the $SO_3^{2-}$-driven reactions (see Supplementary Fig. 8a) and explain the observation of all belt-sulphurs being labelled with Se upon unlimited, high-flux turnover with $SeO_3^{2-}$ (see Fig. 3c). It is interesting to note that the insertion of $SO_3^{2-}$ as belt-sulphur(s) during nitrogenase catalysis is mirrored by the insertion of $SO_3^{2-}$ as a 9$^{th}$ belt-sulphur of the cofactor during nitrogenase assembly.[30–32] While the identity and mobilization of the *in vivo* sulphur source for nitrogenase catalysis and assembly are yet to be fully elucidated, the crucial importance of sulphur mobilization in these processes—an emerging theme that also gained theoretical support from a recent DFT study[33]—points to a potential co-metabolism of nitrogen and sulphur in nitrogen-fixing microorganisms (also see Supplementary Fig. 7). The work reported herein provides a useful tool for uncoupling the contributions of the sulphur- and electron-sources to the reactivity of nitrogenase, which could be instrumental in the further investigation and recalibration of the mechanistic model of this important, yet enigmatic metalloenzyme.

## Methods

Unless otherwise specified, all chemicals were purchased from Sigma-Aldrich (St. Louis, MO). All experiments were performed under an Ar atmosphere using Schlenk techniques and a glove box operating at <3 ppm $O_2$. Aqueous solutions of europium(II) ethyleneglycol-bis(2-aminomethylether)-*N*,*N*,*N*',*N*'-tetraacetic acid ($Eu^{II}$-EGTA) were prepared immediately before use as described earlier.[34]

### Cell growth and protein purification.

*A. vinelandii* strains YM13A (expressing a His-tagged MoFe protein and a non-tagged Fe protein) and YM34A (expressing a His-tagged Fe protein and a non-tagged MoFe protein) were grown in 180 L batches in a 200 L New Brunswick fermenter (New Brunswick Scientific) in Burke's minimal medium supplemented with 2 mM ammonium

acetate. The growth rate was monitored by cell density at 436 nm using a Spectronic 20 Genesys spectrophotometer (Thermo Fisher Scientific). Cells were grown at 30°C until they entered the late exponential phase ($OD_{436}$~1.0), followed by harvest using a flow-through centrifugal harvester (Cepa). The cell paste was washed with a buffer containing 50 mM Tris-HCl (pH 8.0). Published methods were used for the purification of His-tagged MoFe protein (Av1) and non-tagged Fe protein (Av2) in the presence of dithionite,[35,36] or adapted for the purification of His-tagged Av2 or His-tagged Av1* inside an anaerobic glovebox in the absence of dithionite as described previously (see below).[18,37]

### Preparation of $N_2$- or $^{15}N_2$-bound Av1*.

The $N_2$-bound Av1* was prepared using a protocol adapted from the previously published methods.[18,35,37] Specifically, YM13A was grown in 180-L batches as described above, followed by re-suspension of the harvested cells in an anaerobic, but dithionite-free buffer containing 25 mM Tris-HCl (pH 8.0), 500 mM NaCl and 10% (v/v) glycerol, and removal of cell debris by centrifugation in the absence of oxygen.[35] The supernatant was then stirred under $N_2$ in an anaerobic chamber (Vacuum Atmosphere) at an $O_2$ level of <2 ppm for 30 min and then loaded on a Ni-NTA column (GE Healthcare) that was pre-equilibrated with an anaerobic, dithionite-free buffer containing 25 mM Tris-HCl (pH 8.0), 500 mM NaCl and 10% (v/v) glycerol.[37] The remaining steps of the purification were carried out in anaerobic, dithionite-free buffers in an anaerobic chamber as described previously.[35]

The $^{15}N_2$-bound Av1* was prepared by inoculating YM13A into 5 × 2 L flasks, each sealed with rubber caps and containing 1 L Burke's minimum medium supplemented with 2 mM ammonium acetate. The headspace of each flask was first filled with neat $O_2$, and then displaced partially with $^{15}N_2$ to achieve an $O_2$-to-$^{15}N_2$ ratio of approximately 1-to-4. The cells were grown at 30°C until the cell density reached an $OD_{436}$ of ~1.0, when they were harvested by centrifugation. The $^{15}N_2$-bound Av1* was purified in the absence of dithionite as described above for the $N_2$-bound Av1*.

### Turnover of $N_2$-bound Av1* in dithionite.

Av1*(TOD), or Av1* subjected to turnover with dithionite, was prepared by mixing 0.5 mg/mL of $N_2$-bound Av1* with 1 mg/mL Av2, 20 mM dithionite, 5 mM ATP, 52.5 mM $MgCl_2$, 300 mM phosphocreatine, and 1.35 mg/mL phosphocreatine kinase in a total volume of 180 mL. The mixture was stirred for 10 min under $N_2$ in an anaerobic chamber (Vacuum Atmosphere) at an $O_2$ level of <2 ppm, followed by purification of Av1*(TOD) on a Ni-NTA column (GE Healthcare) pre-equilibrated with an anaerobic buffer containing 25 mM Tris-HCl (pH 8.0), 5 mM dithionite, 500 mM NaCl and 10% (v/v) glycerol.

### Turnover of $N_2$-bound Av1* with sulphite or selenite in Eu(II)-EGTA.

Av1*(TOS), or Av1* subjected to turnover with sulphite, was prepared by mixing 0.5 mg/mL of $N_2$-bound Av1* with 1 mg/mL dithionite-free Av2, 10 mM Eu(II)-EGTA, 20 mM sodium sulphite, 5 mM ATP, 52.5 mM $MgCl_2$, 300 mM phosphocreatine, and 1.35 mg/mL phosphocreatine kinase in a total volume of 180 mL. Av1*(TOSe), or Av1* subjected to turnover with selenite, was prepared by mixing 0.5 mg/mL of $N_2$-bound Av1* with 1 mg/mL dithionite-free Av2, 10 mM Eu(II)-EGTA, 2 mM sodium selenite, 5 mM ATP, 52.5

mM $MgCl_2$, 300 mM phosphocreatine, and 1.35 mg/mL phosphocreatine kinase in a total volume of 180 mL. Each mixture was stirred for 10 min at room temperature under $N_2$ in an anaerobic chamber (Vacuum Atmosphere) with an $O_2$ level of <2 ppm, followed by purification of Av1*(TOS) or Av1*(TOSe) on a Ni-NTA column (GE Healthcare) pre-equilibrated with an anaerobic, dithionite-free buffer containing 25 mM Tris-HCl (pH 8.0), 500 mM NaCl and 10% (v/v) glycerol.

### Preparation of dithionite-free Av2.

The non-tagged Av2 was first purified in the presence of dithionite and subsequently passed twice through a Sephadex G25 desalting column to remove dithionite; whereas the His-tagged Av2 was purified directly in the absence of dithionite inside an anaerobic glovebox as described for Av1*.[18] For each experiment, the protein was freshly prepared and immediately used after preparation. The specific activities of the dithionite-free Av2 proteins used in this study are shown in Supplementary Fig. 9. The non-tagged Av2 was used in all experiments that required repurification of His-tagged Av1; whereas the His-tagged Av2 was used in all other experiments.

### Activity assays.

The activity assays of purified Av1* were carried out using a protocol adapted from that published previously.[36] Each assay contained, in a total volume of 1 mL, 0.5 mg Av1*, 5 mg dithionite-free Av2, 25 mM Tris-HCl (pH 8.0), 10 mM Eu(II)-DTPA, 5 mM ATP, 52.5 mM $MgCl_2$, 300 mM phosphocreatine, and 1.35 mg/mL phosphocreatine kinase. 20 mM sodium sulphite or 2 mM sodium selenite was added to the assay to initiate the reaction, which was then allowed to run for 5 min at 30°C. Published methods were used to determine $H_2$ and $C_2H_4$.[38] $NH_4^+$ was determined by a high-performance liquid chromatography fluorescence method.[39] The method for the routine determination of $NH_4^+$ involves the formation of a fluorescent product upon reaction of $NH_4^+$ with OPT (*o*-phthalaldehyde dissolved in ethanol with added mercaptoethanol), followed by detection of this product by a fluorescence detector coupled to a Waters HPLC system, and quantification of $NH_4^+$ by standard curves using known concentrations of ammonia.

### GC and GC–MS analyses of deuterium incorporation into $C_2H_4$.

The deuterium incorporation experiments were carried out using a protocol adapted from that published previously.[27] Specifically, each reaction contained, in a total volume of 1 mL, 1 mg Av1 or Av1*, 8 mg Av2, 25 mM Tris-HCl (pH 8.0), 20 mM dithionite, 5 mM ATP, 52.5 mM $MgCl_2$, 300 mM phosphocreatine, and 1.35 mg/mL phosphocreatine kinase. The reaction mixture was incubated at 30°C for 30 min under a gas atmosphere of 5% $C_2H_2$, 45% $D_2$ and 50% Ar (for Av1*) or 50% $N_2$ (for Av1). Published methods were used to analyse $C_2H_4$ and $C_2H_3D$ by GC and GC-MS analyses.[40,41]

### Frequency-selective pulse NMR analysis of $NH_4^+$ formation.

Preparation of $^{14}N_2$- or $^{15}N_2$-bound Av1* was carried out as described above. The single-turnover reaction contained, in a total volume of 1.5 mL, 15 mg Av1* or Av1, 15 mg Av2, 25 mM Tris-HCl (pH 8.0), 20 mM dithionite and 125 mM ATP. The reaction mixture was

incubated at 30°C for 30 min under a gas atmosphere of 100% Ar, followed by transfer of the mixture to a 1.5 mL tube containing a Microcon centrifugal filter of a MWCO of 10 K (Millipore) and removal of proteins by centrifugation at 10000 g for 20 min. Subsequently, 0.5 mL of the flow through was combined with 0.05 mL of 1M $H_2SO_4$ and 0.025 mL of $CD_3CN$ as a lock agent. The $^1H$ NMR spectra were recorded using a Bruker DRX500 spectrometer equipped with a TCI cryoprobe. Water suppression was employed, and the spectra was referenced by setting the residual $CH_3CN$ signal to 2.06 ppm.[42] 7168 scans were recorded per sample with an acquisition time of 1.5 s and a relaxation delay of 5 s.

### Analysis of $^{15}N_2$ release by GC–MS.

The release of $^{15}N_2$ was determined for the $^{15}N_2$-bound Av1* either as prepared (see above) or upon turnover with sodium sulphite or sodium selenite. The latter samples were prepared by subjecting the freshly prepared $^{15}N_2$-bound Av1* immediately to turnover with sodium sulphite or sodium selenite in Eu(II)-EGTA as described above for the $N_2$-bound Av1*, although the reaction was carried out in a reduced total volume of 30 mL in both cases. After the reaction, Av1*(TOS) or Av1*(TOSe) was reclaimed on a Ni-NTA column (GE Healthcare) pre-equilibrated with an anaerobic buffer containing 25 mM Tris-HCl (pH 8.0), 500 mM NaCl and 10% (v/v) glycerol.

For GC–MS analysis, a total of 15 mg of Av1*, Av1*(TOS) or Av1*(TOSe) was transferred to a sealed, 300-μL vial under Ar prior to addition of 10% trichloroacetic acid to release the bound $^{15}N_2$. The headspace of the acid-quenched sample was then measured by GC–MS, using a Thermo Scientific Trace 1300 GC system coupled to a Thermo ISQ QD (Thermo Electron North America LLC). Specifically, $N_2$ was separated on a TG-BOND Msieve 5A column (30 m × 0.32 mm ID × 30 μm film; Thermo Electron North America LLC), which was held at 45°C for 2 min, heated to 150°C at a rate of 25°C/min, and held at 150°C for 2 min. The carrier gas, He, was passed through the column at a rate of 2.5 mL/min. The mass spectrometer was operated in electron impact ionization (EI) mode, performing both the scanning of the full mass range and the selective ion monitoring (SIM) at an *m/z* ratio of 30. Injection of a blank from a vial containing only Ar was repeated multiple times to establish a background of the ambient surroundings. All traces presented were subtracted with this blank, which was <5% of the injected standard.

### Analysis of $H_2^{34}S$ release by GC–MS.

Av1*(TO$^{34}$S), or Av1* subjected to turnover with $^{34}$S-labeled sulphite ($^{34}SO_3^{2-}$), was prepared by mixing 5 mg/mL of $N_2$-bound Av1* with 10 mg/mL of dithionite-free Av2, 10 mM Eu(II)-EGTA, 10 mM $^{34}$S-labeled sodium sulphite (Sigma-Aldrich), 50 mM ATP, 525 mM $MgCl_2$, 300 mM phosphocreatine, and 1.35 mg/mL phosphocreatine kinase in a total volume of 20 mL. The reaction mixture was stirred for 10 min at room temperature under $N_2$ in an anaerobic chamber (Vacuum Atmosphere) with an $O_2$ level of <2 ppm, followed by purification of Av1*(TO$^{34}$S) on a Ni-NTA column (GE Healthcare) in the absence of dithionite as described for Av1*(TOS) above. 45 mg of purified Av1*(TO$^{34}$S) was mixed with 90 mg of dithionite-free Av2, 10 mM Eu(II)-EGTA, 20 mM sodium sulphite, 50 mM ATP, 525 mM $MgCl_2$, 300 mM phosphocreatine, and 1.35 mg/mL phosphocreatine kinase in a total volume of 9 mL. To ensure completion of the reaction, the mixture was stirred for

60 min at room temperature under $N_2$ in an anaerobic chamber (Vacuum Atmosphere) with an $O_2$ level of <2 ppm, followed by purification of Av1*($TO^{34}S$)$^{60\ min}$ on a Ni-NTA column (GE Healthcare) in the absence of dithionite. Following purification, 25 mg of Av1*($TO^{34}S$) or Av1*($TO^{34}S$)$^{60\ min}$ was subjected to a small-scale M-cluster extraction procedure as described previously,[10] but with the omission of dithionite.

For GC–MS analysis, a total of 15 mg of Av1*($TO^{34}S$) or Av1*($TO^{34}S$)$^{60\ min}$, or ~75 nmol of Av1*($TO^{34}S$)- or Av1*($TO^{34}S$)$^{60\ min}$-extracted M-cluster was treated with 30% trifluoracetic acid in a sealed 300-uL vial. The acid-treated sample was incubated at 60°C for 15 min to volatilize $H_2S$ before the entire headspace was injected by a gas-tight syringe into a GC–MS (Thermo-Fisher Scientific Trace 1300 GC connected to a Thermo-Fisher Scientific ISQ QD single quadrupole mass spectrometry) equipped with a Restek Rxi-1ms column (30 m, 0.32 mm ID, 4.0 μm df). The GC inlet and oven were maintained at a temperature of 30°C, and the mass spectrometry transfer line and ion source were maintained at a temperature of 250 °C. Total ion chromatograms were generated under SIM conditions in the EI mode, and $H_2{}^{34}S$ was detected at an *m/z* ratio of 36.

### Time-dependent $C_2H_2$ reduction with a nitrogenase-free extract as the sulphur source.

A nitrogenase-free extract (NFE) was prepared during the purification of the His-tagged Av1*, where the Av1*-free flow-through was collected from the Ni-NTA column. The $C_2H_2$ reduction assay with the - NFE was performed in the presence of Eu(II)-EGTA and excess Av2 as described above for that with $SO_3^{2-}$, with $SO_3^{2-}$ replaced by 0.3 mL of NFE (31 mg/mL) and the activity measured at 5-, 10-, 20-, 30-, 40-, 50-, and 60-min. The negative control with NFE showed <2% background activity.

### Electron inventory of the $SO_3^{2-}$-driven reaction.

The pre-reduced Av2 was prepared by treating Av2 with 5 mM Eu(II)-EGTA, followed by removal of excess Eu(II)-EGTA using a Sephadex G25 desalting column. Subsequently, the activity assay was conducted, with each assay containing, in a total volume of 10 mL, 10 mg pre-reduced Av2, 1.5 mg Av1*, 25 mM Tris-HCl (pH 8.0), 5 mM ATP, 52.5 mM $MgCl_2$, 300 mM phosphocreatine, 1.35 mg/mL phosphocreatine kinase, and 20 mM sodium sulphite. The reaction mixture was incubated at 30°C for 5 min and subsequently analysed for products. The oxidation of the pre-reduced Av2 was monitored by measuring the absorbance at 425 nm ($[Fe_4S_4]^{2+}$) at the beginning and the end of the assay, which allowed calculation of the concentration of the oxidized Av2 on the basis of the difference of A425 before and after the reaction and an extinction coefficient of $6000 M^{-1}cm^{-1}$ as previously described.[43] The Electron input was then calculated based on a supply of 2 electrons upon oxidation of each pre-reduced, all-ferrous Av2; whereas the electron output was calculated based on the assumption that 3 electrons were consumed for the production of each $NH_3$ and 2 electrons were consumed for the production of each $H_2$.

### ICP-OES determination of the Se/Mo ratios of the extracted M-clusters.

Av1*(TOS) and Av1*(TOSe) were prepared as described above under high electron fluxes. In addition, an M-cluster deficient Av1 (designated $Av1^{apo}$)[44] was prepared with selenite as described for the preparation of Av1*(TOSe), except that Av1* was substituted with $Av1^{apo}$

in the assay. Contrary to Av1*(TOS) and Av1*(TOSe), Av1*(TOSe)$^{N_2}$ was generated with a limited electron flux under $N_2$ to mimic the conditions used to generate Av1*. Specifically, His-tagged Av1 and non-tagged Av2 were first purified in the presence of dithionite and subsequently passed twice through a Sephadex G25 desalting column to remove dithionite from each sample. Subsequently, 1 mg/mL dithionite-free Av1 was combined with 0.5 mg/mL of dithionite-free Av2, 10 mM Eu(II)-EGTA, 2 mM sodium selenite, 5 mM ATP, 52.5 mM $MgCl_2$, 300 mM phosphocreatine, and 1.35 mg/mL phosphocreatine kinase in a total volume of 200 mL and incubated under $N_2$ at 30°C for 5 min, followed by re-isolation of Av1 using a Ni-NTA column. The M-clusters were extracted from 150 mg Av1*, Av1*(TOS), Av1*(TOSe) and Av1*(TOSe)$^{N_2}$, respectively, as described previously.[10] ICP-OES analyses of the Se and Mo contents of the extracted M-clusters were then performed using a published protocol.[32] Standard curves for Se and Mo were generated using the commercially available elemental Se standard (1000 ppm, Sigma-Aldrich) between 0.1 and 1 ppm and the Mo standard between 0.01 and 0.1 ppm, The elemental contents of each sample were adjusted using those of the Av1$^{apo}$ sample as a background control.

### Data Availability

The authors declare that all data supporting the findings of this study are available within the article and its Supplementary Information files or from the corresponding authors upon reasonable request. The structural data related to this work are available at the Worldwide Protein Data Bank (http://www.wwpdb.org) with PDB accession codes 7MCI, 6UG0 and 6VXT.

## Supplementary Material

Refer to Web version on PubMed Central for supplementary material.

## Acknowledgements

This work was supported by NIH-NIGMS grant GM141046 (to Y.H. and M.W.R.). We are grateful to Dr. Philip R. Dennison, Director of the NMR Facility at UC Irvine, for his kind help on the frequency-selective NMR analysis of our samples. We also thank the staff at the Stanford Synchrotron Radiation Lightsource, SLAC National Accelerator Laboratory, Beamline 12–2 (X-ray diffraction) and Beamlines 7–3 and 9–3 (X-ray absorption spectroscopy) for technical support on data collection. Use of the Stanford Synchrotron Radiation Lightsource, SLAC National Accelerator Laboratory, is supported by the U. S. Department of Energy, Office of Science, Office of Basic Energy Sciences under Contract No. DE-AC02-76SF00515. The SSRL Structural Molecular Biology Program is supported by the U. S. Department of Energy, Office of Biological and Environmental Research, and by the National Institutes of Health, National Institutes of General Medical Sciences (P30GM133894).

## REFERENCES

1. Burgess BK & Lowe DJ Mechanism of molybdenum nitrogenase. Chem. Rev. 96, 2983–3012 (1996). [PubMed: 11848849]
2. Buscagan TM & Rees DC Rethinking the nitrogenase mechanism: activating the active site. Joule 3, 2662–2678 (2019). [PubMed: 32864580]
3. Rutledge HL & Tezcan FA Electron transfer in nitrogenase. Chem. Rev. 120, 5158–5193 (2020). [PubMed: 31999100]
4. Jasniewski AJ, Lee CC, Ribbe MW & Hu Y Reactivity, mechanism, and assembly of the alternative nitrogenases. Chem. Rev. 120, 5107–5157 (2020). [PubMed: 32129988]

5. Hu Y, Lee CC & Ribbe MW Extending the carbon chain: hydrocarbon formation catalysed by vanadium/molybdenum nitrogenases. Science 333, 753–755 (2011). [PubMed: 21817053]
6. Lee CC, Hu Y & Ribbe MW Vanadium nitrogenase reduces CO. Science 329, 642 (2010). [PubMed: 20689010]
7. Seefeldt LC et al. Reduction of substrates by nitrogenases. Chem. Rev. 120, 5082–5106 (2020). [PubMed: 32176472]
8. Einsle O & Rees DC Structural enzymology of nitrogenase enzymes. Chem. Rev. 120, 4969–5004 (2020). [PubMed: 32538623]
9. Spatzal T et al. Evidence for interstitial carbon in nitrogenase FeMo cofactor. Science 334, 940 (2011). [PubMed: 22096190]
10. Wiig JA, Hu Y, Lee CC & Ribbe MW Radical SAM-dependent carbon insertion into the nitrogenase M-cluster. Science 337, 1672–1675 (2012). [PubMed: 23019652]
11. Lowe DJ & Thorneley RNF The mechanism of *Klebsiella pneumoniae* nitrogenase action. Pre-steady-state kinetics of $H_2$ formation. Biochem. J. 224, 877–886 (1984). [PubMed: 6395861]
12. Lowe DJ & Thorneley RNF The mechanism of *Klebsiella pneumoniae* nitrogenase action. The determination of rate constants required for the simulation of the kinetics of $N_2$ reduction and $H_2$ evolution. Biochem. J. 224, 895–901 (1984). [PubMed: 6395863]
13. Thorneley RNF & Lowe DJ The mechanism of *Klebsiella pneumoniae* nitrogenase action. Pre-steady-state kinetics of an enzyme-bound intermediate in $N_2$ reduction and of $NH_3$ formation. Biochem. J. 224, 887–894 (1984). [PubMed: 6395862]
14. Thorneley RNF & Lowe DJ The mechanism of *Klebsiella pneumoniae* nitrogenase action. Simulation of the dependences of $H_2$-evolution rate on component-protein concentration and ratio and sodium dithionite concentration. Biochem. J. 224, 903–909 (1984). [PubMed: 6395864]
15. Lee SC, Lo W & Holm RH Developments in the biomimetic chemistry of cubane-type and higher nuclearity iron-sulphur clusters. Chem. Rev. 114, 3579–3600 (2014). [PubMed: 24410527]
16. Spatzal T, Perez KA, Einsle O, Howard JB & Rees DC Ligand binding to the FeMo-cofactor: structures of CO-bound and reactivated nitrogenase. Science 345, 1620–1623 (2014). [PubMed: 25258081]
17. Spatzal T, Perez KA, Howard JB & Rees DC Catalysis-dependent selenium incorporation and migration in the nitrogenase active site iron-molybdenum cofactor. Elife 4, e11620 (2015). [PubMed: 26673079]
18. Kang W, Lee CC, Jasniewski AJ, Ribbe MW & Hu Y Structural evidence for a dynamic metallocofactor during $N_2$ reduction by Mo-nitrogenase. Science 368, 1381–1385 (2020). [PubMed: 32554596]
19. Yates MG The enzymology of molybdenum-dependent nitrogen fixation. In Biological Nitrogen Fixation (Stacey G, Burris RH & Evans HJ, eds) pp. 685–735, Chapman & Hall, New York (1992).
20. Jensen BB & Burris RH Effect of high $pN_2$ and high $pD_2$ on $NH_3$ production, $H_2$ evolution, and HD formation by nitrogenases. Biochemistry 24, 1141–1147 (1985). [PubMed: 3913463]
21. Li JL & Burris RH Influence of $pN_2$ and $pD_2$ on HD formation by various nitrogenases. Biochemistry 22, 4472–4480 (1983). [PubMed: 6354256]
22. Burgess BK, Wherland S, Newton WE & Stiefel EI Nitrogenase reactivity: insight into the nitrogen-fixing process through hydrogen-inhibition and HD-forming reactions. Biochemistry 20, 5140–5146 (1981). [PubMed: 6945872]
23. Wherland S, Burgess BK, Stiefel EI, Newton WE Nitrogenase reactivity: effects of component ratio on electron flow and distribution during nitrogen fixation. Biochemistry 20, 5132–5140 (1981). [PubMed: 6945871]
25. Lowe DJ & Thorneley RN The mechanism of *Klebsiella pneumoniae* nitrogenase action. The determination of rate constants required for the simulation of the kinetics of $N_2$ reduction and $H_2$ evolution. Biochem. J. 224, 895–901 (1984). [PubMed: 6395863]
26. Chatt J Chemistry relevant to the biological nitrogen fixation of nitrogen. In Nitrogen Fixation (Stewart WDP & Gallon JR, eds) pp. 1–18, Academic Press, London (1980).
27. Yang Z-Y et al. On reversible $H_2$ loss upon $N_2$ binding to FeMo-cofactor of nitrogenase. Proc. Natl. Acad. Sci. USA 110, 16327–16332 (2013). [PubMed: 24062454]

28. Nielander AC et al. A versatile method for ammonia detection in a range of relevant electrolytes via direct nuclear magnetic resonance techniques. ACS Catal. 9, 5797–5802 (2019).
29. Sippel D et al. A bound reaction intermediate sheds light on the mechanism of nitrogenase. Science 359, 1484–1489 (2018). [PubMed: 29599235]
30. Tanifuji K et al. Tracing the incorporation of the “ninth sulfur” into the nitrogenase cofactor precursor with selenite and tellurite. Nat. Chem.13, 1228–1234 (2021). [PubMed: 34635813]
31. Jasniewski AJ et al. Spectroscopic characterization of an eight-iron nitrogenase cofactor precursor that lacks the “9$^{th}$ sulphur”. Angew. Chem. Int. Ed. Engl. 58, 14703–14707 (2019). [PubMed: 31411369]
32. Tanifuji K et al. Tracing the “ninth sulphur” of the nitrogenase cofactor via a semi-synthetic approach. Nat. Chem. 10, 568–572 (2018). [PubMed: 29662207]
33. Wei WJ & Siegbahn PEM A mechanism for nitrogenase including loss of a sulphide. Chemistry 28, e202103745 (2022). doi: 10.1002/chem.202103745. [PubMed: 35098591]
34. Vincent KA et al. Instantaneous, stoichiometric generation of powerfully reducing states of protein active sites using Eu(II) and polyaminocarboxylate ligands. Chem. Commun. 20, 2590–2591 (2003).
35. Ribbe MW, Hu Y, Guo M, Schmid B & Burgess BK The FeMoco-deficient MoFe protein produced by a *nifH* deletion strain of *Azotobacter vinelandii* shows unusual P-cluster features. J. Biol. Chem. 277, 23469–23476 (2002). [PubMed: 11978793]
36. Burgess BK, Jacobs DB & Stiefel EI Large-scale purification of high activity *Azotobacter vinelandii* nitrogenase. Biochim. Biophys. Acta. 614, 196–209 (1980). [PubMed: 6930977]
37. Lee CC, Ribbe MW & Hu Y Purification of nitrogenase proteins. Methods Mol. Biol. 1876, 111–124 (2019). [PubMed: 30317477]
38. Gavini N & Burgess BK FeMo cofactor synthesis by a *nifH* mutant with altered MgATP reactivity. J. Biol. Chem. 267, 21179–21186 (1992). [PubMed: 1400428]
39. Corbin JL Liquid chromatographic-fluorescence determination of ammonia from nitrogenase reactions: a 2-min assay. Appl. Environ. Microbiol. 47, 1027–1030 (1984). [PubMed: 16346533]
40. Lee CC, Hu Y, & Ribbe MW Tracing the hydrogen source of hydrocarbons formed by vanadium nitrogenase. Angew. Chem. Int. Ed. Engl. 50, 5545–5547 (2011). [PubMed: 21538750]
41. Lee CC, Hu Y & Ribbe MW Reduction and condensation of aldehydes by the isolated cofactor of nitrogenase. ACS Cent. Sci. 4, 1430–1435 (2018). [PubMed: 30410981]
42. Fulmer GR et al. NMR chemical shifts of trace impurities: common laboratory solvents, organics, and gases in deuterated solvents relevant to the organometallic chemist. Organometallics 29, 2176–2179 (2010).
43. Wiig JA, Hu Y, & Ribbe MW NifEN-B complex of *Azotobacter vinelandii* is fully functional in nitrogenase FeMo cofactor assembly. Proc. Natl. Acad. Sci. USA 108, 8623–8627 (2011). [PubMed: 21551100]
44. Schmid B et al. Structure of a cofactor-deficient nitrogenase MoFe protein. Science 296, 352–356 (2002). [PubMed: 11951047]

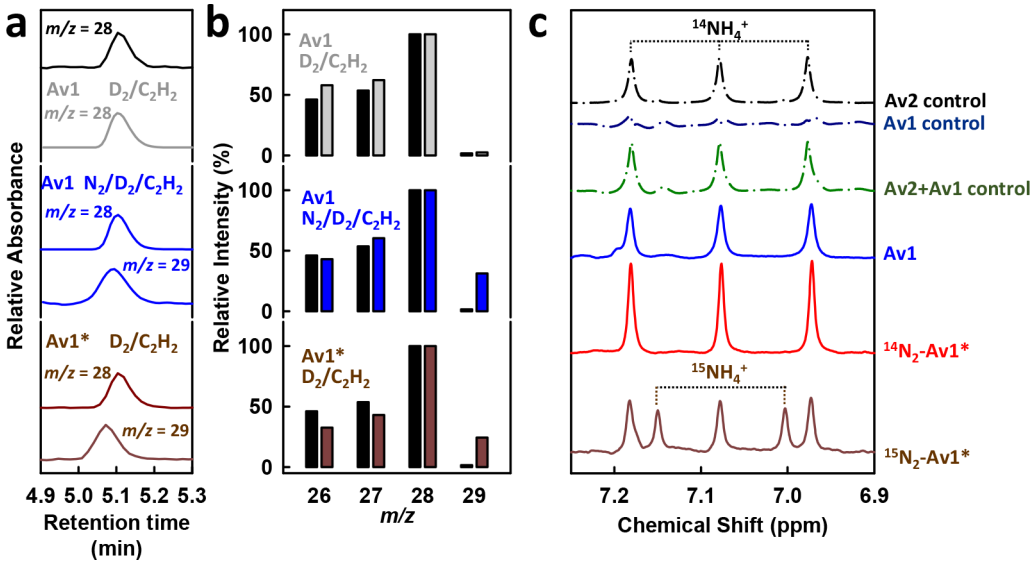


**Fig. 1. GC-MS and frequency-selective NMR analyses of $N_2$-bound Av1*.**

(**a**) GC elution profiles and (**b**) GC-MS fragmentation patterns of $C_2H_4$ generated upon turnover with Av1 under $D_2/C_2H_2$ (grey), Av1 under $N_2/D_2/C_2H_2$ (blue), and Av1* under $D_2/C_2H_2$ (brown) in $H_2O$-based reactions. The $C_2H_4$ standard is shown as black dashed lines (in a) and black bars (in b). The *m*/*z* ratio is indicated for each trace. (**c**) Frequency-selective $^1H$ NMR spectra of $NH_4^+$ generated from Av1 (solid blue), Av1* prepared with $^{14}N_2$ (solid red) and Av1* prepared with $^{15}N_2$ (solid brown) upon turnover under Ar in the presence of Av2, MgATP and dithionite. Also shown are the $^1H$ NMR spectra of Av2 control (dashed black) and Av1 control (dashed blue), generated with only Av2 and only Av1, respectively, under Ar in the presence of MgATP and dithionite, as well as a sum of the two, Av1+Av2 control (dashed green). All samples in a-c contained the same amount of Av1, Av1* and/or Av2. Note the minor bumps in the NMR spectra that likely resulted from degraded proteins or interactions of proteins with reagents.

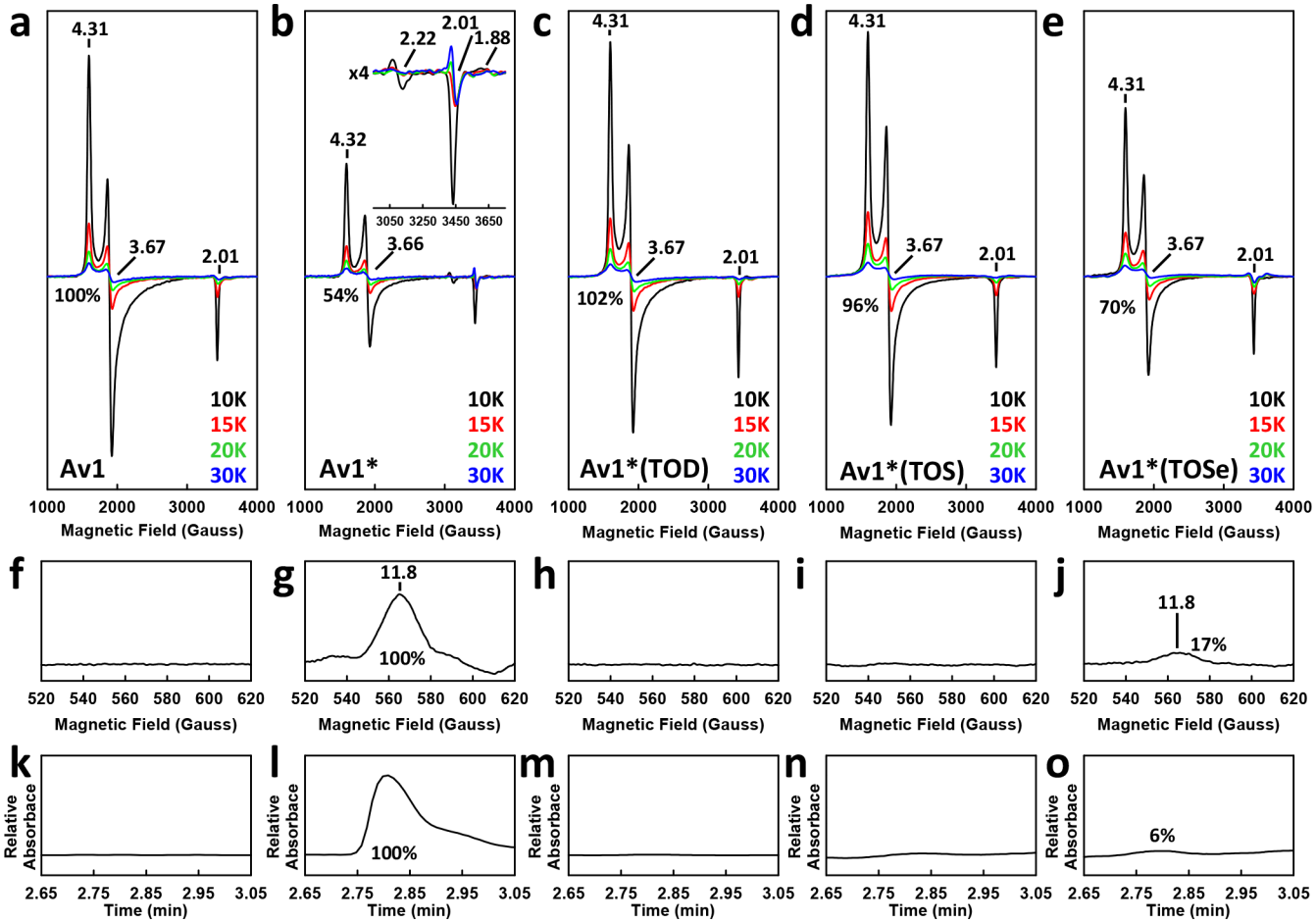


**Fig. 2. EPR and GC-MS analyses of various Av1 protein species.**

Shown are the perpendicular (**a-e**) and parallel (**f-j**) mode EPR spectra of the resting-state Av1 (a, f), the $N_2$-bound Av1* (b, g), the dithionite-reactivated Av1*(TOD) (c, h), the Eu(II)-EGTA/sulphite-reactivated Av1*(TOS) (d, i), and the Eu(II)-EGTA/selenite-reactivated Av1*(TOSe) (e, j). Reactivation of Av1* with dithionite, Eu(II)-EGTA/sulphite, or Eu(II)-EGTA/selenite was achieved under turnover conditions in the presence of Av2 and ATP. The perpendicular-mode spectra (a-e) were recorded at 10K (black), 15K (red), 20K (green) and 30K (blue) using a microwave power of 20 mW. Previously unobserved features appeared in the $S = 1/2$ region of the spectrum of Av1* at $g = 2.22$ (maximized at 10K) and $g = 2.01$ and 1.88 (maximized at 30K), respectively (b, inset, 4x enlarged). The relative intensities of the M-cluster-specific $S = 3/2$ signals are indicated, with the signal intensity of Av1 set at 100%. The parallel-mode spectra (f-j) were recorded at 10K using a microwave power of 50 mW. The relative intensities of the $P^{OX}$-specific signal at $g = 11.8$ are indicated, with the signal intensity of Av1* set at 100%. (**k-o**) GC-MS analysis of $^{15}N_2$ released upon acid quenching of Av1 (k), Av1* (l), Av1*(TOD) (m), Av1*(TOS) (n), and Av1*(TOSe) (o). $^{15}N_2$ was traced at $m/z = 30$.

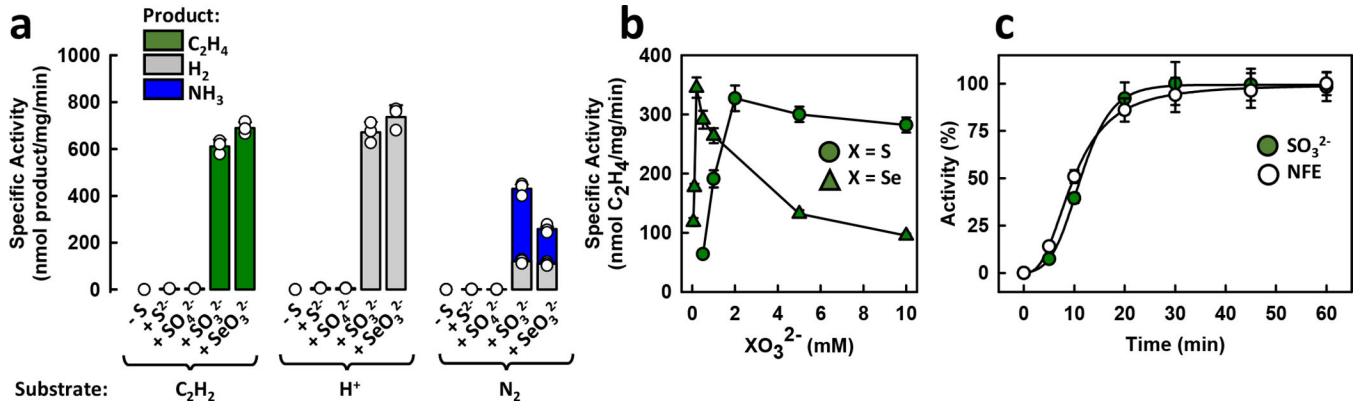


**Fig. 3. Requirement of sulphite-type species for substrate turnover.**

(**a**) Activities of Av1* in *in vitro* activity assays containing Av2, MgATP and Eu(II)-EGTA in the absence −S) or presence of various sulphur sources ($+S^{2-}$, $+SO_4^{2-}$ and $+SO_3^{2-}$) or selenite ($+SeO_3^{2-}$). (**b**) Titration of the $C_2H_2$-reducing activity of Av1* *versus* increasing concentrations of sulphite ($SO_3^{2-}$) or selenite ($SeO_3^{2-}$) in *in vitro* assays containing Av2, MgATP and Eu(II)-EGTA. (c) Time-dependence of the activity of Av1* in $C_2H_2$ reduction using 2 mM $SO_3^{2-}$ (green solid circles) or nitrogenase-free extract (designated NFE; open circles) as a sulphur source. 318±36 and 250±16 nmol $C_2H_4$/mg were generated in assays containing $SO_3^{2-}$ and NFE, respectively. Data in a-c are expressed as mean ± s.d. (n=3 independent experiments).

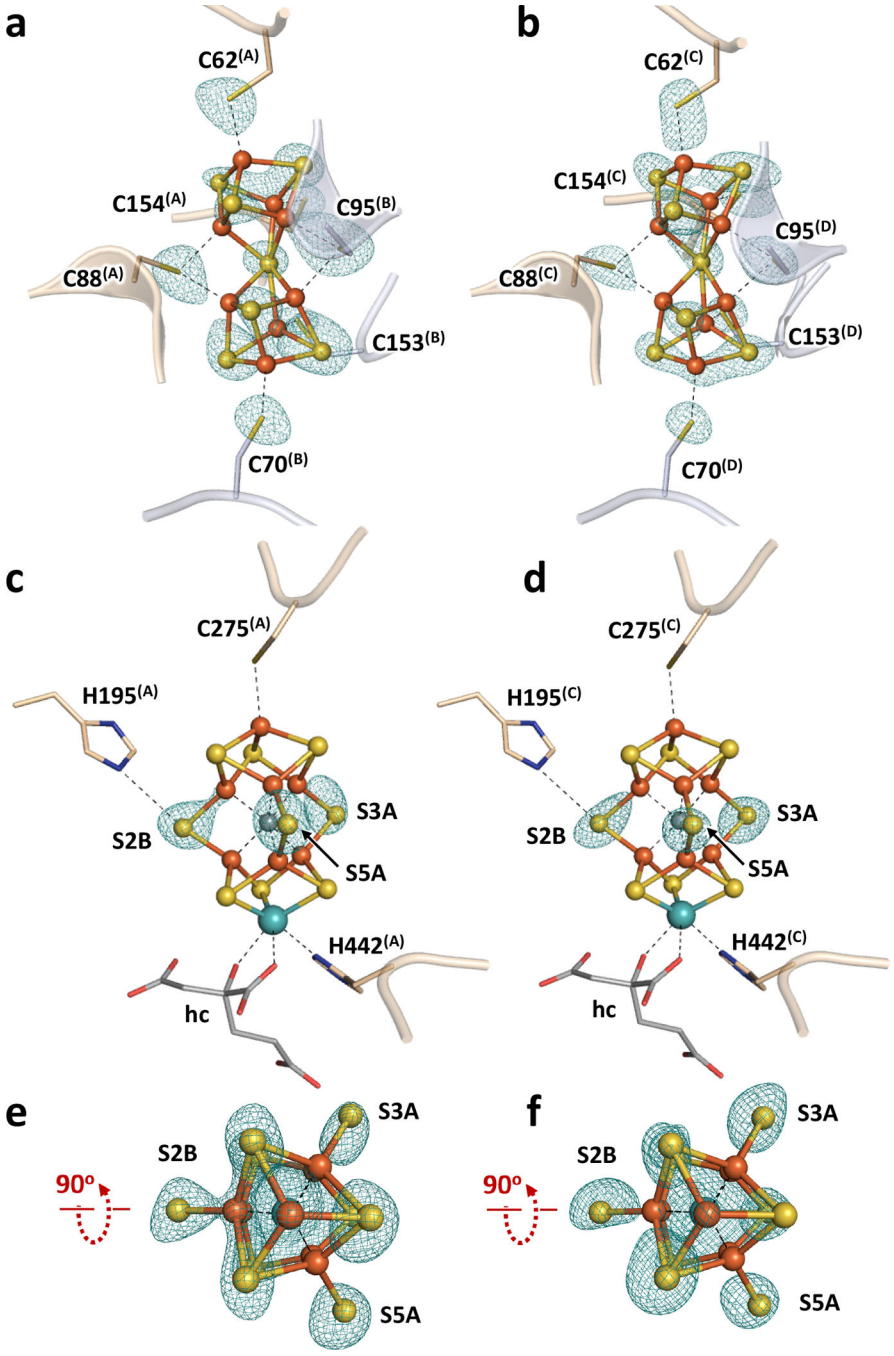


**Fig. 4. Crystallographic analysis of Av1*(TOS).**

(**a**, **b**) Structures of P-clusters at the interface of (a) Chain-A/B (P-cluster$^{(A/B)}$) and (b) Chain-C/D (P-cluster$^{(C/D)}$) of Av1*(TOS), overlaid with the anomalous density maps (mint-blue mesh) calculated at 7100 eV at 2.00 Å resolution and contoured at 5.0 σ. Chain-A and Chain-C are the α-subunit, and Chain-B and Chain-D the β-subunits, of the two αβ-dimers of Av1*. The P-clusters are illustrated in ball-and-stick presentation, and their ligands are shown as sticks. Chain-A and Chain-C are illustrated as wheat ribbons, and Chain-B and Chain-D are shown as light-blue ribbons. Colour code of atoms: Fe, orange; S, yellow;

O, red; N, blue. (**c-f**) Structures of M-clusters in (c, e) Chain-A (M-cluster$^{(A)}$) and (d, f) Chain-C (M-cluster$^{(C)}$), refined at 1.65 Å resolution. (c, d) Side view and (e, f) view along the Fe1-C-Mo axis of (c, e) M-cluster$^{(A)}$ and (d, f) M-cluster$^{(C)}$, overlaid with the anomalous density maps (mint-blue mesh) calculated at 7100 eV at 2.00 Å resolution and contoured at 5.0 $\sigma$. The key residues that interact with the clusters are shown as sticks.

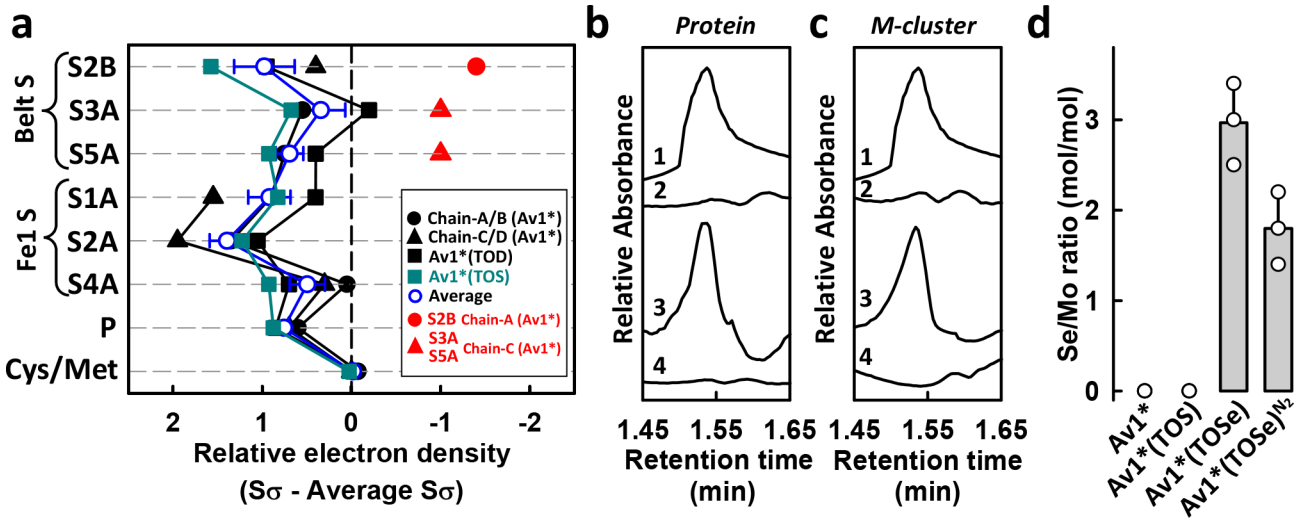


**Fig. 5. Catalysis-dependent mobilization of belt sulphurs.**

(**a**) Relative electron densities of individual sulphurs or sulphur groups in various Av1 proteins or protein chains. The relative electron density (solid circle, triangle or rectangle) is expressed as the difference between the sigma level of an individual sulphur or sulphur group (Sσ) and the average sigma level of all sulphurs in the protein (average Sσ). The average densities of individual sulphurs or sulphur groups in all structures depicted in this graph (open blue circles) are expressed as mean ± s.e.m. (n=4 independent biological samples for Fe1 S and Cys/Met; and n=3 for Belt S). Designations: Belt S, sulphurs at the belt region of the M-cluster; Fe1 S, sulphurs ligated to Fe1 of the M-cluster; P, sulphurs in the P-clusters; Cys/Met, sulphurs in the Cys and Met residues. PDB entries: Av1*, 6UG0;[18] Av1*(TOD), 6VXT;[18] Av1*(TOS), 7MCI (this work) (**b, c**) GC-MS analysis of the release of the acid labile, cluster-bound $^{34}S^{2-}$ ions in Av1*(TOS) (b) and its isolated M-clusters (c) as $H_2{}^{34}S$. Shown are (1) $H_2S$ standard, (2) Av1*(TOS), (3) Av1*(TOS) upon turnover with excess $^{34}SO_3^{2-}$ for 10 min [designated Av1*(TO$^{34}$S)], and (4) Av1*(TO$^{34}$S) upon turnover with excess unlabelled $^{32}SO_3^{2-}$ for 60 min [designated Av1*(TO$^{34}$S)$^{60\ min}$]. $H_2{}^{34}S$ was traced at *m/z* = 36. **(d)** ICP-OES determination of Se/Mo ratios of the M-clusters extracted from Av1*, Av1*(TOS), Av1*(TOSe) and Av1*(TOSe)$^{N_2}$. Data in d are expressed as mean ± s.d. (n=3 independent experiments).

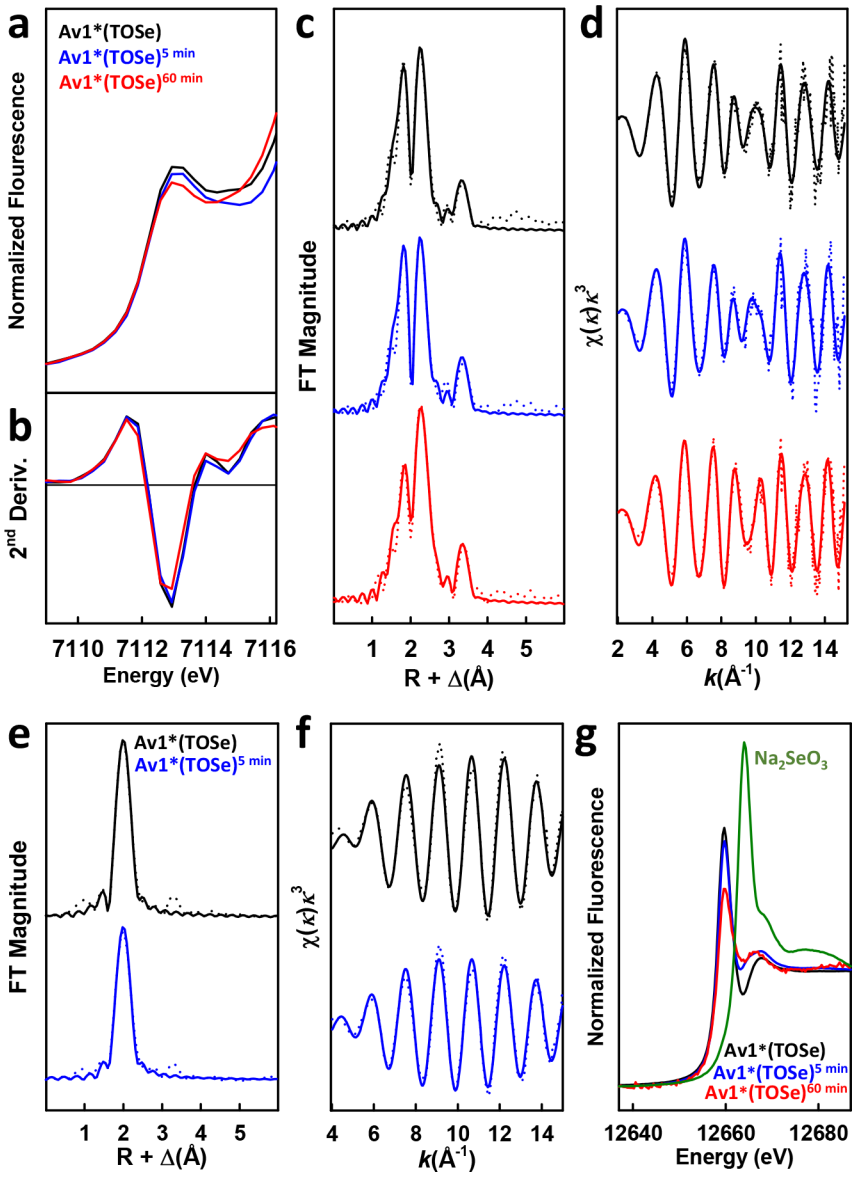


**Fig. 6. XAS/EXAFS analysis of Av1*(TOSe).**

(**a-d**) Fe and (**e-g**) Se K-edge XAS analyses of Av1*(TOS) upon turnover with excess $SeO_3^{2-}$ for 10 min [designated Av1*(TOSe); black], Av1*(TOSe) upon turnover with excess $SO_3^{2-}$ for 5 min [designated Av1*(TOSe)$^{5\ min}$, blue], and Av1*(TOSe) upon turnover with excess $SO_3^{2-}$ for 60 min [designated Av1*(TOSe)$^{60\ min}$, red]. Shown for the Fe K-edge analysis are (a) the pre-edge regions of the normalized fluorescence spectra and (b) smoothed second derivatives of the pre-edge regions, (c) the Fourier transforms of the EXAFS data (dotted) and the best fits of data (solid), and (c) the $k^3$-weighted EXAFS data (dotted) and the best fits of data (solid). Shown for the Se K-edge analysis are (e) the Fourier transforms of the EXAFS data (dotted) and the best fits of data (solid), (f) the $k^3$-weighted EXAFS data (dotted) and the best fits of data (solid), and (g) the spectra of the rising edges compared to the $Na_2SeO_3$ standard (dark green). See Supplementary Tables 3–6 and

Supplementary Tables 7–9, respectively, for detailed fits of the Fe and Se K-edge EXAFS data.

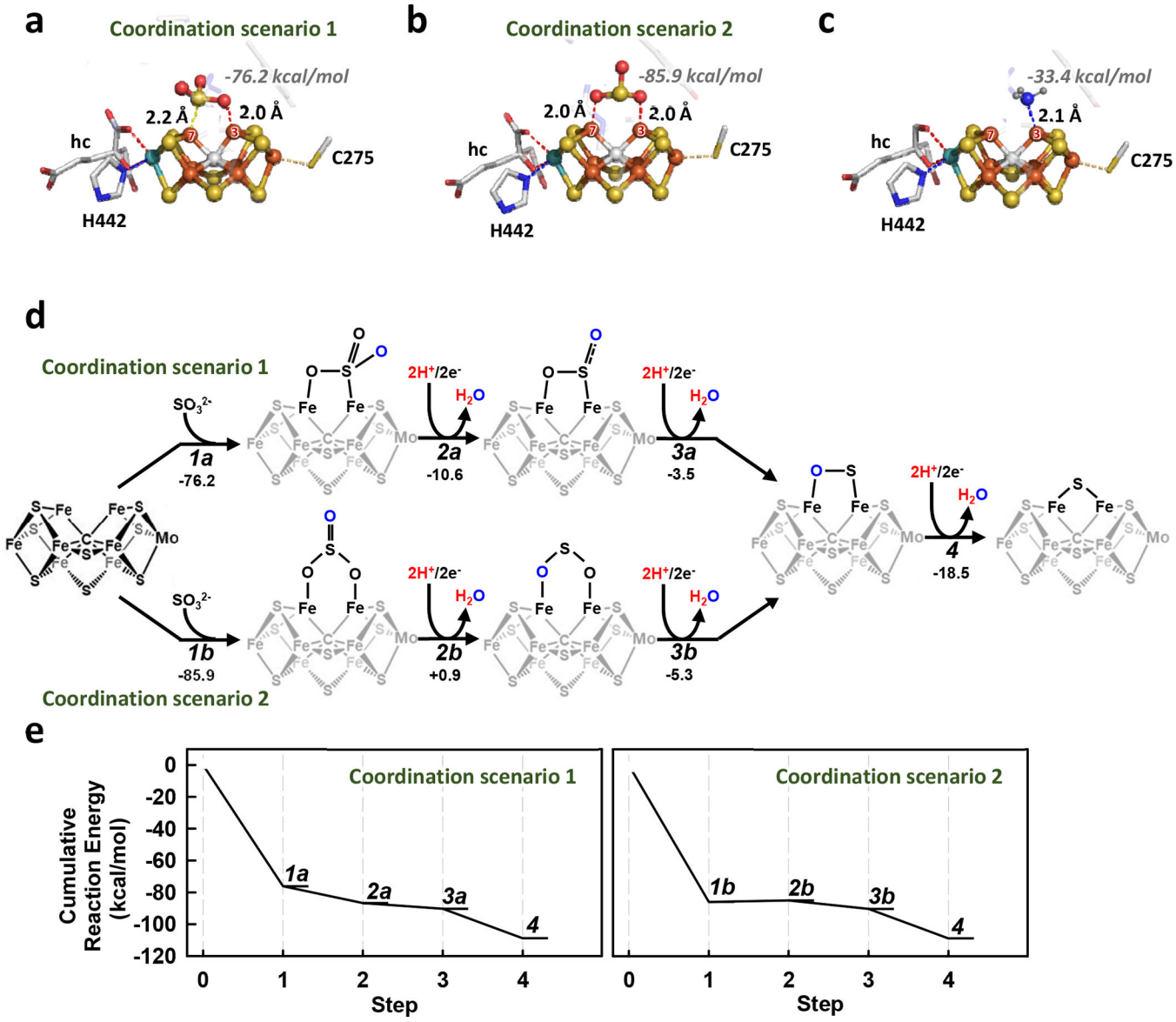


**Fig. 7. Coordination and reduction of $SO_3^{2-}$.**

(**a-c**) DFT-optimized models of the M-cluster coordinated by $SO_3^{2-}$ or $NH_3$. DFT models of the M-clusters (taken from PDB entry 6VXT)[18] with and without ligands were optimized with TPSS-D3/def2-SV(P). Coordination energies were obtained by calculating single point energies (TPSS-D3/def2-TZVP) for the optimized structures. $SO_3^{2-}$ is bridged between Fe3 and Fe7 either via its S atom and one of its O atoms (a, coordination scenario 1), or via two of its O atoms (b, coordination scenario 2), at the S5A site; whereas $NH_3$ is coordinated asymmetrically by Fe3 at the same site (c). The M-cluster and the coordinating ligands ($SO_3^{2-}$ or $NH_3$) are shown in ball-and-stick presentation. The residues used for the model are shown as sticks. The atoms are coloured as described in Fig. 4. (**d**) Reaction energies of the two coordination scenarios of $SO_3^{2-}$ derived from DFT calculations (TPSS/def2-TZVP, COSMO ε=20, DFT-D3) on the M-cluster models, assuming that coupled $e^-/H^+$ transfer takes place after the initial coordination step. The energies (kcal/mol) for both pathways

(coordination scenario 1: steps 1a, 2a, 3a and 4; coordination scenario 2: Steps 1b, 2b, 3b and 4) are indicated in the scheme. (**e**) Cumulative reaction energies of sulphur incorporation for the two coordination scenarios of $SO_3^{2-}$.